



Universiteit
Leiden
The Netherlands

Exploring charge transport properties and functionality of molecule-nanoparticle ensembles

Devid, E.J.

Citation

Devid, E. J. (2015, December 17). *Exploring charge transport properties and functionality of molecule-nanoparticle ensembles*. *Casimir PhD Series*. Retrieved from <https://hdl.handle.net/1887/37091>

Version: Not Applicable (or Unknown)

License: [Leiden University Non-exclusive license](#)

Downloaded from: <https://hdl.handle.net/1887/37091>

Note: To cite this publication please use the final published version (if applicable).

Cover Page



Universiteit Leiden



The handle <http://hdl.handle.net/1887/37091> holds various files of this Leiden University dissertation.

Author: Devid, Edwin Johan

Title: Exploring charge transport properties and functionality of molecule-nanoparticle ensembles

Issue Date: 2015-12-17

5

The influence of molecular mobility on the properties of gold nanoparticle organic ligand networks

We prepare and investigate two-dimensional (2D) single layer arrays and multilayered networks of gold nanoparticles derivatized with conjugated hetero-aromatic molecules, i.e. S-(4-([2,6-(bipyrazol-1-yl)pyrid-4-yl]ethynyl)phenyl)thioate. This ligand molecule is used to cap the gold nanoparticles and will be referred to as S-BPP. The structures are fabricated by a combination of self-assembly and microcontact printing techniques, and are characterized by electron microscopy, UV-Vis spectroscopy and Raman spectroscopy. Selective binding of the S-BPP molecules to the gold nanoparticles via Au-S bonds is found, with no evidence for the formation of Au-N bonds between pyridine or pyrazole groups from the BPP and the gold surface. Subtle, but significant shifts with temperature of specific Raman S-BPP modes are also observed. These modes attribute to dynamic changes in the orientation and/or increased mobility of the molecules on the gold nanoparticle facets. As for their conductance, the temperature-dependence for S-BPP networks differs significantly from standard alkanethiol-capped networks, especially above 220 K. When relating the latter two observations, it appears that dynamic changes in the molecular layers effectively lower the molecular tunnel barrier for S-BPP-based arrays at higher temperatures.

5.1 Introduction to molecular ligand-nanoparticle ensembles

Inspired by nature, self-assembly is a bottom-up method to fabricate structures at all scales from nanometer-sized ingredients. In this way, new functional materials can be created with properties that are, in principle, based on the specific functionality of their building blocks [1]. An interesting approach, used for molecular conductance experiments, includes nanoparticles (~10 nm) incorporated to bridge the size gap between macroscopic electrodes (≥ 100 nm) and molecules (~1 nm) [2-8]. Typically, 2D arrays of gold nanoparticles capped by alkanethiols are created, after which dithiolated conjugated molecules are allowed to form molecular bridges between neighbouring nanoparticles [6, 8]. Although molecular insertion cannot be driven to completeness for thermodynamic reasons [9, 10], this protocol has proven successful in molecular electronics, e.g. by providing access to switchable molecular devices [11, 12]. The process can also be used for non-thiol ligands [13]. This Chapter extends the self-assembly procedure of arrays beyond alkanes, by making use of an attractive class of molecular ligands.

Molecules of the tridentate 2,6-bi(pyrazolyl)pyridine (BPP) group are well known to act as weak σ -donor/ π -acceptor ligands exhibiting octahedral coordination environment with coordination number 6 for transition metals [14]. Moreover, for the case of iron (II) ions, the S-BPP-ligands adjust the ligand field strength to access the so-called spin transition (ST) or spin crossover (SCO) regime [15], in which the physical properties depend strongly on their intrinsic low- and high-spin states (LS ($S = 0$) and HS ($S = 2$)) state. Integrated ST units may be considered as potential electronic components in the construction of switching molecular devices [16, 17], a vision for which the control of the attaching of S-BPP-units to gold nanoparticles sets the stage. Towards this goal, the synthetic introduction of substituents at the 4'-position of the pyridine moiety of BPP has been shown to be a useful strategy. In particular the introduction of highly conductive π -conjugated phenylethynyl linker moieties with acetyl protected thiol anchoring groups facilitates contact to noble and coinage metal electrodes [18].

In this study, we report on the fabrication of 2D single layer ligand-gold nanoparticle arrays (and multilayer ligand-gold nanoparticle networks) formed by gold nanoparticles covered by planar aromatic organic ligand-based S-BPP molecules. The inclusion of the thioacetate end group (see AcS-BPP molecule in Figure 5.1) [18] is

expected to steer the adsorption of the S-BPP molecule to the gold nanoparticles [19]. The results of the structural and spectroscopic characterization of the synthesized 2D ligand-gold nanoparticle arrays (in short Au-NP-S-BPP-arrays), by means of UV-Vis and electron microscopy (SEM, HR-TEM and 3D TEM) experiments, will be presented. Specifically, surface-enhanced Raman spectroscopy (SERS) provides insight into the selectivity of the bond formation. Remarkably, Raman experiments also reveal subtle shifts in some S-BPP modes related to reversible structural modification within the array induced by temperature. This observation is compared to temperature-dependent transport experiments. For this purpose, the fabricated 2D Au-NP-S-BPP arrays are electrically contacted to lithographically defined devices [5, 8, 9, 12] and the obtained conductance measurements are compared to benchmark networks formed with alkanethiols spacers.

5.2 Capping of gold nanoparticles with S-BPP molecules

To create arrays of S-BPP capped gold nanoparticles, the well-established procedure to make alkanethiol-based nanoparticles arrays [8, 9, 20] is adapted and applied. The first step is the synthesis of citrate stabilized gold nanoparticles in aqueous solvent (see paragraph 3.1.1).

This is followed by centrifuging 5 mL of monodispersed citrate stabilized gold nanoparticle suspension at 15000 RPM for 1 hour. After centrifugation, the aqueous solvent is removed from the settled gold nanoparticles, followed immediately by nanoparticles redispersion in ethanol. Through forceful shaking, the nanoparticles are redispersed quickly to yield a stable colloidal dispersion, sealed in a glass bottle and sonicated in a water bath for approximately an hour.

Functionalization of gold nanoparticles with S-BPP molecules [18] is accomplished in two steps (according to the method described earlier in paragraph 3.3.2). The process of functionalization is accelerated by sonication in a water bath. After 15 minutes, the functionalized gold nanoparticle dispersion has changed colour. As shown below, UV-Vis absorption spectroscopy reveals that this colour change can be attributed to the S-BPP molecule assembling around the gold nanoparticles. Next, the functionalized gold nanoparticles are left to settle down by gravity in a cold, dark storage environment [21, 22] for three days. The supernatant is then removed from the sediment, which is redispersed in 4 mL of chloroform and sonicated for 1 hour. Finally, a lightly purple

coloured dispersion of functionalized gold nanoparticles is used to prepare a self-assembled 2D Au-NP-S-BPP array.

5.3 The fabrication of 2D Au-NP-S-BPP arrays

The 2D single layer Au-NP-S-BPP array is prepared using a Langmuir-Schaefer (LS) method (see Figure 5.1) where a single layer array of functionalized gold nanoparticles is self-assembled at the air/water interface [8, 23, 24]. A Teflon mould, containing a hole, is filled with 300 μL of demineralised Millipore water. Then, 30 μL of S-BPP functionalized gold nanoparticles in chloroform are dispersed on the aqueous layer. The steadily evaporating chloroform leaves the nanoparticles at the air-water interface. The hydrophobically functionalized gold nanoparticles attract each other on the water surface and self-assemble into a highly ordered array. The array is then transferred on a Si wafer substrate (covered with 300 nm of SiO_2) by using a polydimethylsiloxane (PDMS) microcontact printing method [8].

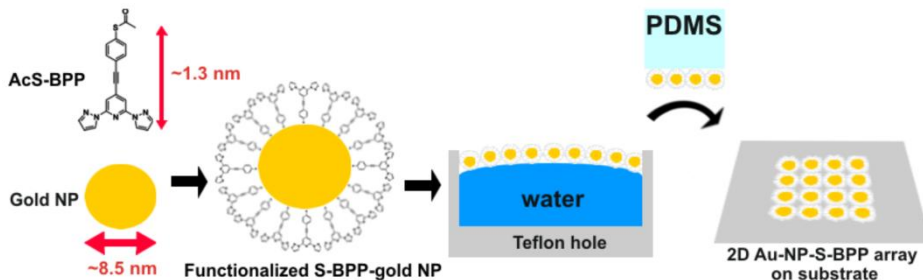


Figure 5.1: Fabrication of 2D Au-NP-S-BPP array (not to scale). The ingredients are gold nanoparticles (diameter 8.5 ± 1.5 nm) and AcS-BPP molecules (length molecule 1.3 nm without the protective acetyl (Ac) group). The arrays are fabricated through self-assembly and then placed onto a substrate of choice by PDMS microcontact printing.

Other suitable types of substrates for microcontact printing these samples are glass, quartz, several types of plastics (like polyethylene, polypropylene foils and polyimide (Kapton) films) and electron beam lithography written high-aspect-ratio (HAR) nanotrench electrodes devices (see Figure 5.2) [25]. The Au-NP-S-BPP arrays are stored in a dark and cold environment and can be kept for several months.

5.4 Imaging of Au-NP-S-BPP arrays and networks

Scanning electron microscopy (SEM) is used to image the arrays on flat (oxidized) silicon substrates and the Au-NP-S-BPP networks on nanotrench electrodes devices (see Figure 5.2).

In general the Au-NP-S-BPP networks are reasonably well ordered. However, single defects and larger voids (as seen in Figure 5.2) will be present too. Although the latter may lead to more complicated percolation paths, conductance properties are expected to be dominated by the more ordered regions. The ordering of an Au-NP-S-BPP network is similar on the SiO₂ substrate and on the Au nanotrench electrodes. The main reason for this is that the Au-NP-S-BPP arrays were self-assembled on water, before actually being transferred to a substrate. Figure 5.3(a) shows a SEM image of a nanoparticle array that was microcontact printed on a SiO₂ substrate. Typically, these Au-NP-S-BPP arrays reveal ordered structures on flat surfaces extending over several hundred nanometers, depending on the microcontact printing procedure used. The nanoparticles have not coalesced and are well separated by the capping ligands S-BPP. Scanning transmission electron microscopy (STEM) and transmission electron microscopy (HAADF-STEM, HR-TEM and 3D TEM) are also used to accurately characterize the nanoscale structuring of multilayered networks on carbon-covered TEM grids. It should be noted that, whereas regular 2D-structures are readily obtained on flat (oxidized) silicon substrates, ordered assembly on the TEM grids turned out to be more challenging, resulting in structures with local order only (see Figure 5.3(b)).

HAADF-STEM images of Au-NP-S-BPP networks (see Figure 5.3(b)) show a fairly uniform distribution of functionalized gold nanoparticles, sometimes as a single layer, but typically a few stacked layers. The latter is probably caused by repeating deposition of Au-NP-S-BPP arrays on the TEM grids by dipping the TEM grids. Microscopic analyses of the network confirm the monodispersity of the gold nanoparticles with average diameter of 8.5 ± 1.5 nm. Moreover, Fast Fourier Transforms (FFT) of the HAADF-STEM images indicate an average particle distance of 10.6 nm. The resulting average next neighbour distance is close to 2 nm, consistent with an expected value between one (1.3 nm) and two (2.6 nm) molecular lengths of S-BPP.

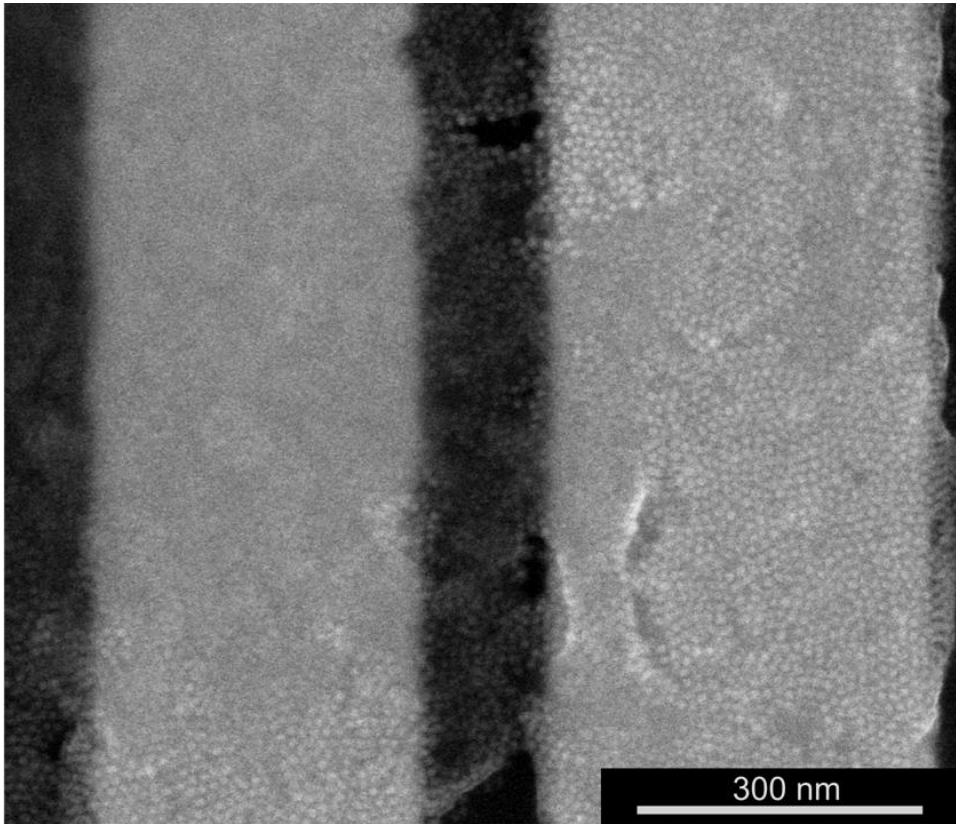


Figure 5.2: SEM image of Au-NP-S-BPP network device for conductance experiments. The two Au electrodes have been defined by electron-beam lithography. The resulting ‘nanotrenches’ of around 120 nm distance between the Au electrodes ensure a favourable aspect ratio for conductance measurements. These Au-NP-S-BPP networks have been obtained via three microcontact printing sequences of Au-NP-S-BPP arrays onto the HAR nanotrench devices.

Figure 5.3(c) shows the energy-dispersive X-ray (EDX) spectrum corresponding to the HAADF-STEM image of the thin Au-NP-S-BPP network film (see Figure 5.3(b)). In addition to Au, the expected spectra of the organic ligand elements C, N and S (partially overlapped by Au) are detected. The oxygen may originate from the presence of water when dipping the TEM grid into the self-assembled Au-NP-S-BPP array on the water.

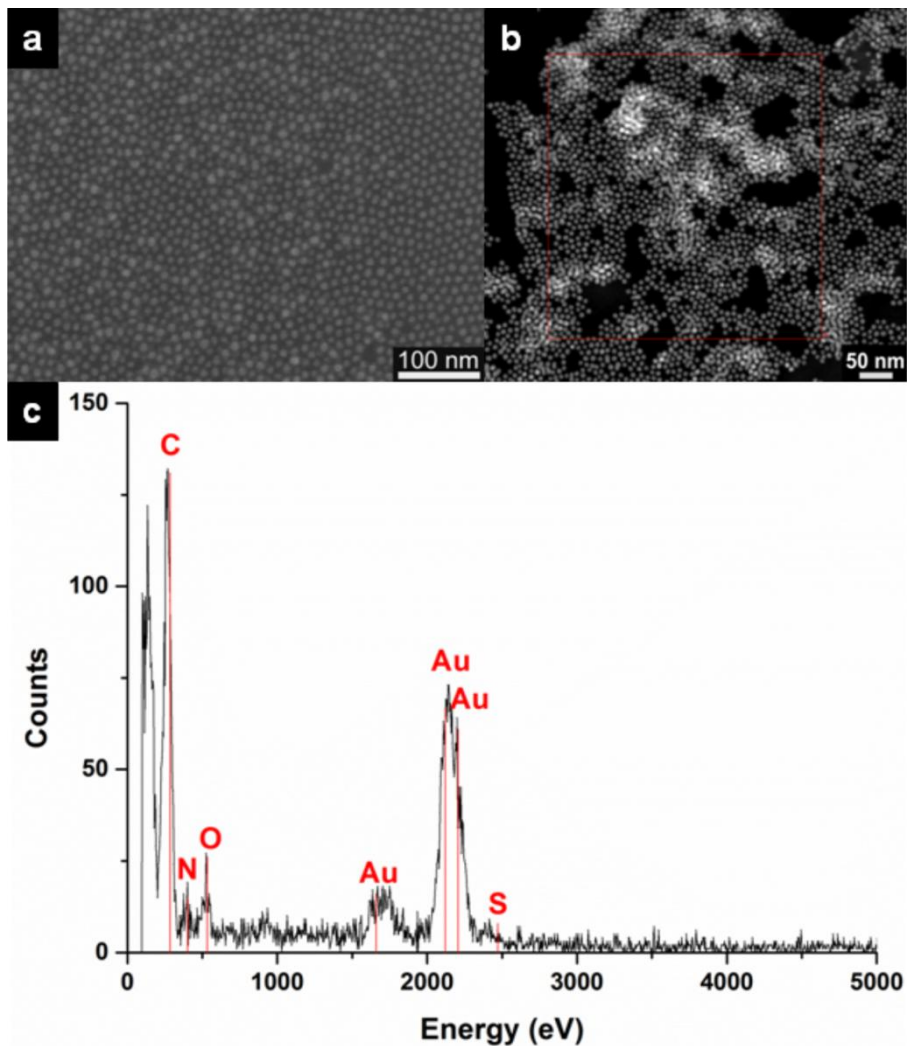


Figure 5.3: Characterization of Au-NP-S-BPP arrays and networks by electron microscopy. (a) SEM image of a 2D single layer microcontact printed Au-NP-S-BPP array on a flat Si-SiO₂ substrate. (b) STEM-reference image of a Au-NP-S-BPP network area on a TEM grid substrate. (c) local EDX analysis revealing the elemental composition.

HAADF-STEM tomography [26, 27] was used to further analyze the spatial packing of multilayered Au-NP-S-BPP networks. From 3D reconstruction of a multilayered Au-NP-S-BPP network, it is indeed observed that the S-BPP functionalized gold

nanoparticles not only form a packed array separated by organic S-BPP molecules in 2D, but also enable sterically driven ordering of gold nanoparticle layers in a partial multi-stack volume.

5.5 UV-Vis spectroscopy on 2D Au-NP-S-BPP arrays

Ultraviolet-visible (UV-Vis) spectroscopy was performed to gain insight into the optical properties of these molecule-gold nanoparticle arrays, and specifically to investigate the influence of the S-BPP molecules on the effective dielectric constant. Metal nanoparticles exhibit absorbance due to surface plasmon resonances (SPR) that occur at frequencies ω (or wavelengths λ) at which the particle's surface charges are oscillating resonantly with the electromagnetic driving field (the incoming photons, see also paragraph 3.5.1). For near-spherical particles, only one SPR mode is expected [28]. According to Mie theory in the dipolar quasi-static approximation (where the diameter d of the nanoparticle is assumed much smaller than the wavelength, i.e. $d \ll \lambda$), the position of the SPR is directly related to the permittivity of the medium surrounding the nanoparticle [29, 30]. In molecule-gold nanoparticle arrays, this permittivity will be largely influenced by the molecules separating the nanoparticles. Hence, Au-NP-S-BPP arrays are expected to have optical properties different from reference alkanethiol-gold nanoparticle arrays. A further influence on the SPR is exerted by the optical interaction of one nanoparticle with the full set of neighbouring gold nanoparticles.

A suitable way to describe the SPR in molecule-gold nanoparticle arrays is via the Maxwell-Garnett theory (again in the quasi-static approximation). This effective medium theory defines an effective dielectric constant of the medium ϵ_{eff} that takes into account both the presence of the surrounding medium and the neighbouring nanoparticles [31-33]. The resonance condition is then given by:

$$\epsilon_1(\omega_{sp})(1 - f) + \epsilon_m(2 + f) = 0. \quad (5.1)$$

Here, ω_{sp} denotes the frequency of the SPR and ϵ_m is the dielectric constant of the medium surrounding the nanoparticles. The so-called filling factor $f = V_{clusters}/V_{total}$ denotes the relative volume occupied by other nanoparticles around the resonating nanoparticle [9]. In this way, the surrounding nanoparticles in an array are incorporated into the theory effectively. Note that for $f = 0$ (i.e., there is no interaction between the nanoparticles) the condition is $\epsilon_1(\omega) = -2\epsilon_m$, as in standard Mie theory.

Figure 5.4 shows the absorption curves for four types of 2D molecule-gold nanoparticle arrays, with alkanethiol-protected gold nanoparticles of various lengths (C8, C10, C12) compared to the 2D Au-NP-S-BPP array. From C8 to C12, the SPR shifts to shorter wavelengths [9], as expected for a blue shift originating from a change in the spacing distance between the gold nanoparticles, i.e. a decrease in filling factor f , (see equation 5.1).

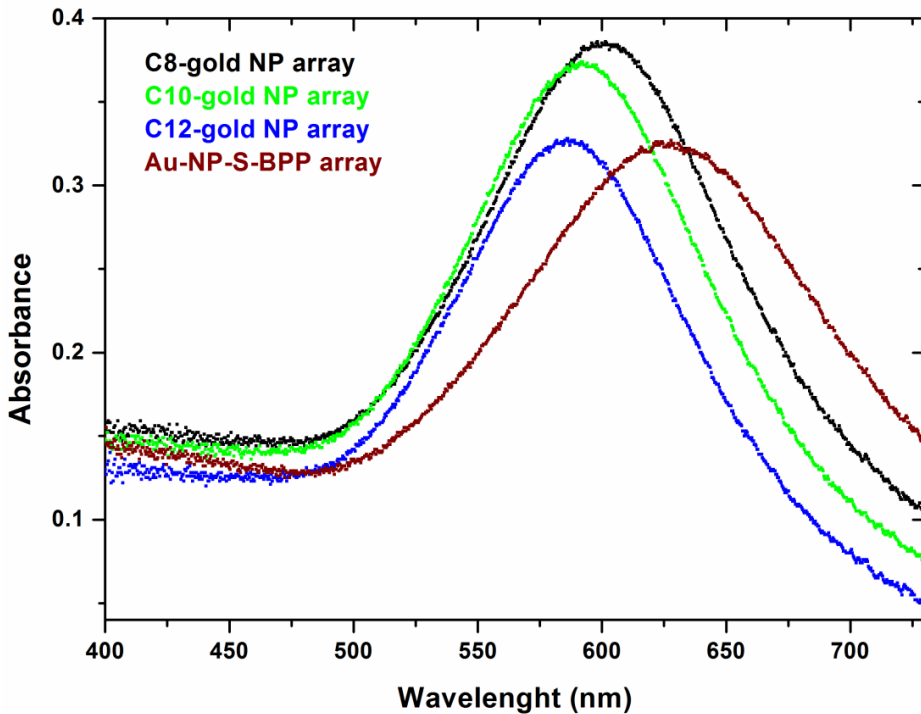


Figure 5.4: UV-Vis (ultraviolet-visible light) spectroscopy of several functionalized gold nanoparticle arrays. Gold nanoparticles are covered by C8 (black), C10 (green), C12 (blue) and S-BPP (red), respectively.

However, the situation is different for the 2D Au-NP-S-BPP array, for which a significant change in ϵ_m is expected, since S-BPP molecules are fully conjugated and hence more easily polarizable. Compared to the alkanethiols-gold nanoparticle arrays, a red shift is indeed observed in Figure 5.4. This is also confirmed experimentally via UV-Vis spectroscopy on a C8-gold nanoparticle dispersion and a S-BPP-gold

nanoparticle dispersion (both in chloroform (i.e. CHCl_3)), where effectively $f = 0$ (see Figure 5.5). Figure 5.5 shows that the SPR peak of the S-BPP-covered gold nanoparticles in CHCl_3 solvent is red-shifted by 17 nm compared to the C8-gold nanoparticle dispersion. Using Mie theory ($f = 0$), the dielectric constants is estimated for the C8-gold nanoparticle dispersion and the S-BPP-gold nanoparticle dispersion to be 2.2 ± 0.1 and 2.8 ± 0.1 , respectively. The results obtained so far can now be checked for consistency.

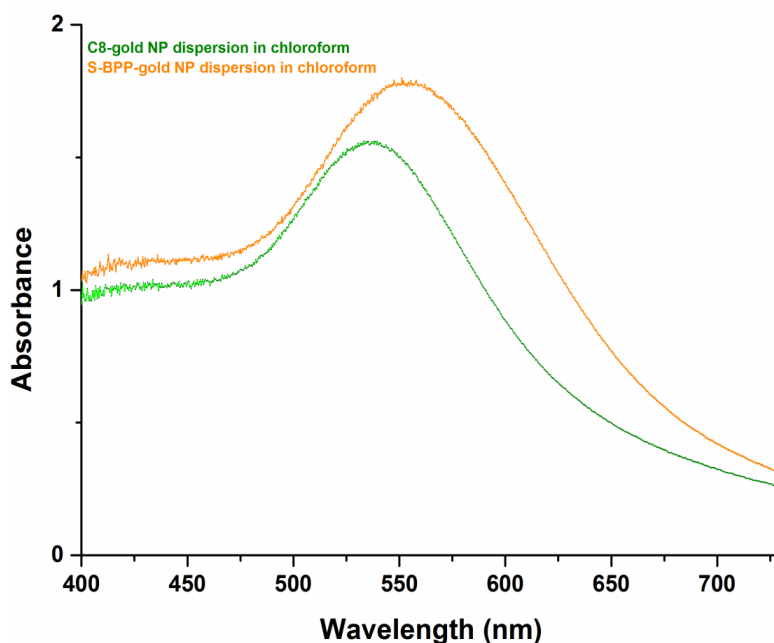


Figure 5.5: UV-Vis spectroscopy of (green) octanethiol functionalized gold nanoparticle dispersion versus (orange) S-BPP-gold nanoparticle dispersion. For both dispersions a chloroform solvent is used.

Since f can be estimated from the electron microscopy images, for both the C8-gold nanoparticle array and the Au-NP-S-BPP array, the Maxwell-Garnett theory can be applied to estimate the dielectric constant ϵ_m in these arrays. The values for ϵ_m within an array or in dispersion are approximately the same values, for both S-BPP molecules and for C8 molecules (see Table 1).

Table 1: Relative dielectric constant due to the ligands ϵ_m (octanethiols versus S-BPP) as calculated from UV-Vis spectra of both nanoparticle dispersions and nanoparticle arrays.

Type functionalized gold nanoparticles	λ_{SP} (nm)	f	Relative dielectric constant ϵ_m
C8-gold nanoparticle dispersion	535.9	0	2.2 ± 0.1
S-BPP-gold nanoparticle dispersion	553.9	0	2.8 ± 0.1
C8-gold nanoparticle array	600.2	0.35	2.4 ± 0.1
Au-NP-S-BPP array	626.0	0.36	2.8 ± 0.1

These values are consistent with values for alkanethiols-gold nanoparticle arrays and oligo(phenylene ethynylene) (OPE)-bridged gold nanoparticle arrays obtained via molecular exchange [9, 30]. For clarity the latter type of molecular exchanged arrays contain a mixture of OPE's and alkanes, unlike the Au-NP-S-BPP arrays.

5.6 Room-temperature Raman spectroscopy on 2D Au-NP-S-BPP arrays

To get more insight into the binding of the S-BPP molecules to the gold as well as to investigate the temperature-dependence of molecular ordering, surface-enhanced Raman spectroscopy on the 2D Au-NP-S-BPP array was performed. In Figure 5.6 the room-temperature Raman spectra of a bulk (powder) sample of AcS-BPP molecules (see Figure 5.6(a)) and of a 2D Au-NP-S-BPP array (see Figure 5.6(b)) are compared. In spite of the much lower concentration of the S-BPP molecule anticipated from the 2D single layer coated array (at least 3 orders of magnitude) compared to the bulk quantity, the Raman spectral intensity is comparable between the two types of samples (see Figure 5.6(a) versus Figure 5.6(b)). Moreover, the Raman spectra from the Au-NP-S-BPP array shows better signal-to-noise ratio attributed to surface enhancement of the Raman signal. The arrayed nature of the gold nanoparticles and their small

interparticle separation leads to a plasmon absorbance shown in Figure 5.4, which is resonant with the 633 nm excitation used here.

Although there are clear commonalities, the spectra of the 2D single layer array (see Figure 5.6(b)) and AcS-BPP powder spectra (see Figure 5.6(a)) exhibit notable differences. The individual spectral features are broader in the SERS spectrum, consistent with the higher heterogeneity in the microenvironment the S-BPP molecules experienced in the array compared to the powder. Furthermore, the SERS spectrum is less complex than that of the powder. This is consistent with plasmonic enhancement as the vibrational modes involving the atoms closest to the gold nanoparticle will be selectively enhanced.

Whereas the low frequency Au-S or Au-N stretch modes cannot be easily discerned from the background in the spectral region below 400 cm^{-1} , it is interesting to note that the thioacetate and acetate modes observed in the solid sample, for example a weak feature at 1698 cm^{-1} (see red arrow in Figure 5.6(a)) assigned to the acetate C=O and features between $1367\text{-}1380\text{ cm}^{-1}$, are no longer evident in the SERS spectrum of the Au-NP-S-BPP arrays. This strongly suggests that the thiol is bound to the gold after surface-mediated hydrolysis of the acetate group. The dominance of key benzenethiol modes in the SERS spectrum is also indicative of binding via thiol moiety. The most intense Raman feature in the powder spectrum of AcS-BPP is the aryl in-plane C-C stretch mode centred at 1591 cm^{-1} . This mode is shifted to 1576 cm^{-1} in the bound S-BPP molecule of the 2D arrays, which matches precisely the in-plane C-C stretch reported for SERS of benzenethiol on copper or silver and is a further indication of binding through sulphur or thioacetate [35, 36].

The second most intense feature in the SERS spectrum is a mode at 1076 cm^{-1} , which is assigned to the aromatic C-S stretch shifted from 1095 cm^{-1} in the powder sample. Both the shift and enhancement of this mode is characteristic of SAMs of benzenethiol on plasmonic metals, and is further evidence that the S-BPP is binding to the gold surface through this moiety [35, 36]. Other characteristic benzenethiol features are also enhanced, at 990, 660 (see red arrow in Figure 5.6(b)) and 406 cm^{-1} .

The alkyne $\text{C}\equiv\text{C}$ stretch mode, which is by far the most intense mode in the powder sample, is reduced in relative intensity in the 2D single layer array, but remains a dominant feature albeit shifted from 2222 to 2211 cm^{-1} on surface binding.

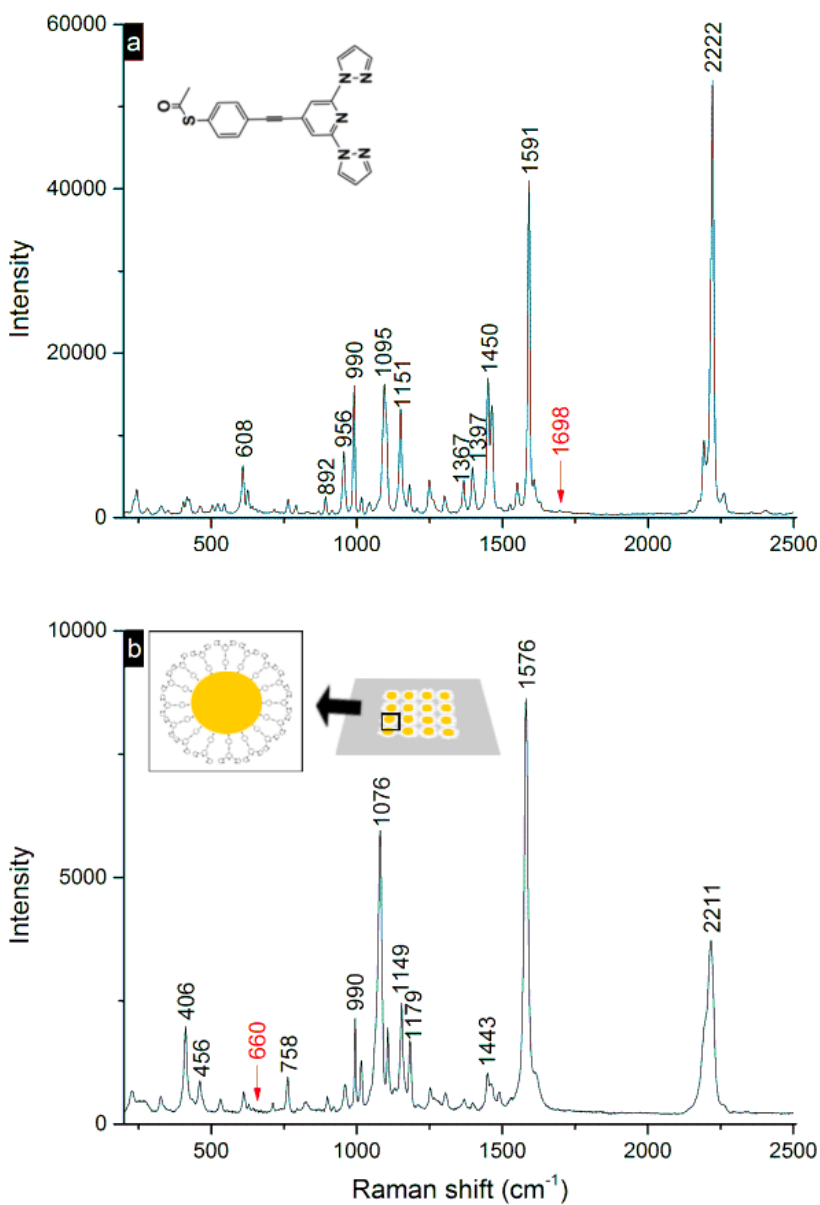


Figure 5.6: (a) Room-temperature Raman spectrum of bulk (powder) AcS-BPP molecules showing 200-2400 cm⁻¹ region excited at 633 nm (1.2 mW illuminating power on the sample). (b) Room-temperature Raman spectrum of 2D (single layer) Au-NP-S-BPP array obtained by microcontact printing on a quartz substrate.

This suggests modest weakening of the C≡C bond presumably induced by binding of the thiol to the surface [37]. By comparison, the Raman modes from the S-BPP moiety are weaker than the benzenethiol moiety in the SAM spectrum. Features at 1443, 1149, 1179 and 785 cm⁻¹ are attributed to the S-BPP, principally to the pyrazole moieties [38]. A weak shoulder centred at 1607 cm⁻¹ is attributed to the pyridine moiety. The low relative intensity of this mode suggests it is not directly bound to the nanoparticle. Overall, the predominance of SERS signal from the benzenethiol moiety and comparatively weaker enhancement of pyrazole modes provides strong evidence that the S-BPP binds to the nanoparticles preferably via the thiol linker.

5.6.1 Temperature-dependent Raman spectroscopy on 2D Au-NP-S-BPP arrays

The 2D Au-NP-S-BPP arrays studied by Raman microscopy over the temperature range 80 to 353 K are shown in Figure 5.7. The absence of significant chemical changes with temperature is indicated by the overall similarity between the spectra under temperature variation. However, some subtle changes can be noticed. Across most of the SERS-enhanced modes, a small shift to the blue of between 2 and 4 cm⁻¹ is observed with decreasing temperature. Interestingly, the unaffected modes are the weakest features in the spectrum, i.e. those that are not strongly SERS enhanced. In other words the bonds nearest the nanoparticle surface are most affected by the changing temperature. This observation suggests that temperature induces changes to bonding interactions between the nanoparticle and the S-BPP. Possible changes are conformational/orientational changes of S-BPP with respect to the nanoparticle surface, which might be expected to cause shifts in the frequencies of bonds close to the nanoparticle. Such electronic changes would also be likely to transmit to chemical moieties conjugated to the bound group [39].

Correspondingly, the most strongly affected modes are the C-C stretch associated with the benzenethiol at 1576 cm⁻¹ at room temperature, which shifts to 1582 cm⁻¹ at 80 K and to 1575 cm⁻¹ at 353 K. The alkyne, C≡C stretch mode is also particularly strongly affected, with shifts from a 2207 cm⁻¹ value at 353 K to 2211 cm⁻¹ at room temperature, and to 2223 cm⁻¹ at 80 K. This mode is broad at 353 K, comprising a main feature and a shoulder at room temperature, which sharpens and resolves at 80 K into a second band at 2190 cm⁻¹.

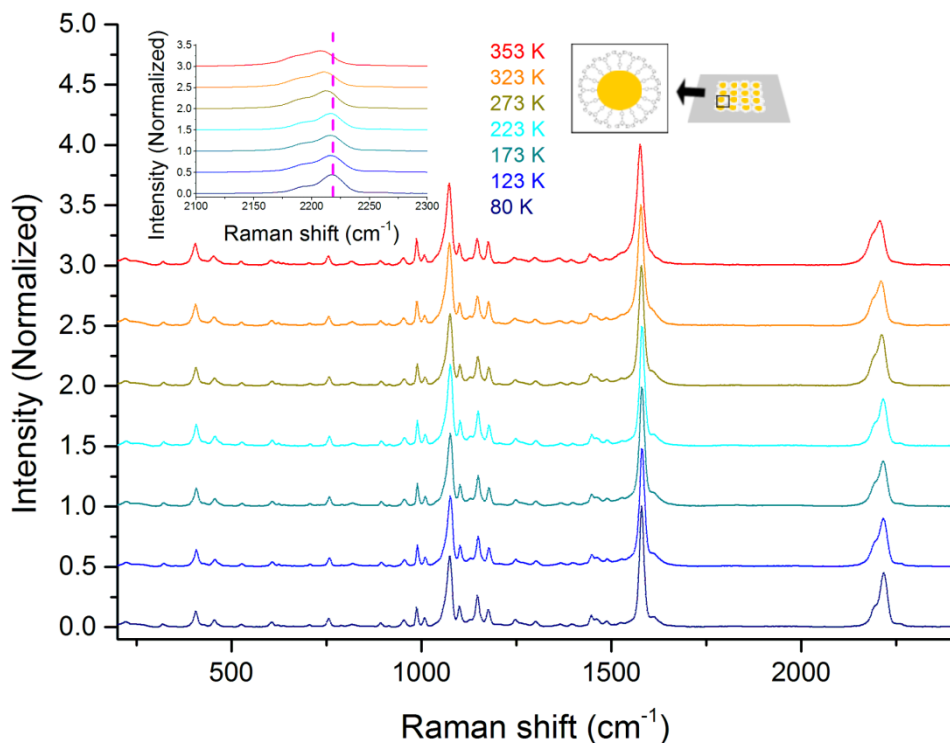


Figure 5.7: Temperature-dependent Raman spectra of 2D Au-NP-S-BPP array microcontact printed on a quartz substrate excited at 633 nm (illuminating power 1.2 mW at the sample). Inset: expansion of the alkyne stretch mode; the vertical marker shows the temperature shifts in the spectra.

As described previously, a significant shift in the $C\equiv C$ stretch mode was observed on thiol binding to the gold surface indicating the significant electronic coupling between the benzenethiol and the surface. It is noteworthy that the $C\equiv C$ stretch mode is so sensitive to temperature in this system, as also found in other reports on Raman of alkynes [37]. Their large polarizability renders them sensitive to electronic changes within their molecular vicinity, particularly in conjugated systems [40, 41]. The surface-bound benzenethiol is sensitive to temperature, but the alkyne exhibits much larger temperature-dependent spectral changes, with a 16 cm^{-1} shift between 80 and 353 K.

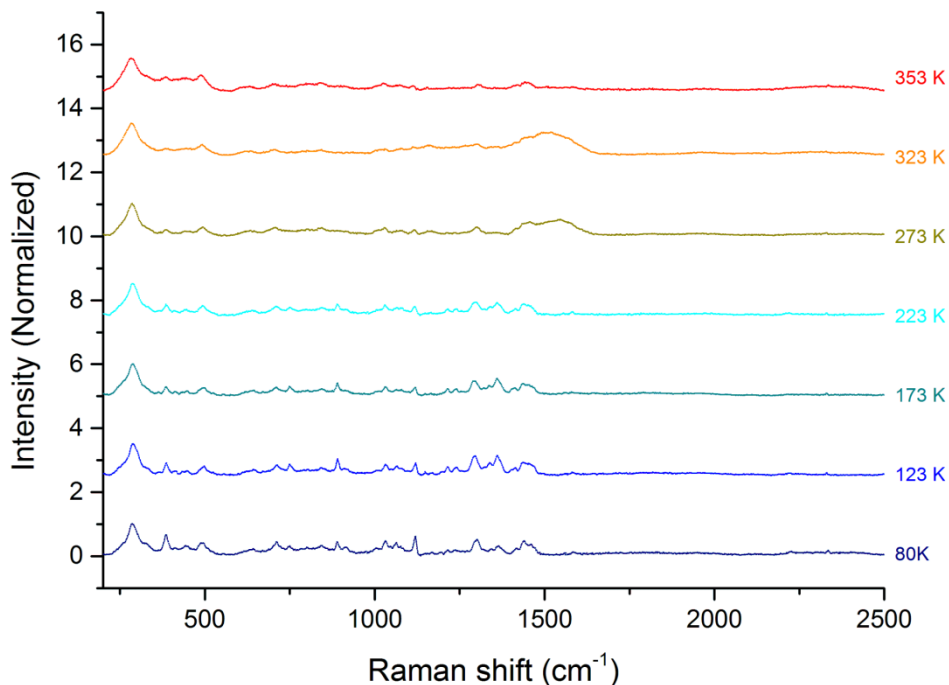


Figure 5.8: Temperature-dependent Raman spectra of octanethiol-gold nanoparticle array, microcontact printed on a quartz substrate excited at 633 nm (illuminating power 1.2 mW at the sample).

This is tentatively attributed to changes in the orientation of the molecule, possibly promoted by Au-S mobility at the surface with temperature. It is important to note that the Raman spectral changes with temperature are fully reversible, i.e. restoring the Au-NP-S-BPP arrays to room temperature following cooling to 80 K lead to recovery of the original room-temperature spectrum across all features. Comparison studies on alkanethiol-modified gold nanoparticle arrays (see Figure 5.8) reveal that temperature changes in their associated Raman spectra are much more modest than those observed for Au-NP-S-BPP arrays. Figure 5.8 shows that the largest shifts observed in individual modes does not typically exceed 2 cm^{-1} and the sharpening (improved resolution) of the vibrational bands, is the main effect of low temperature. This observation appears to validate the hypothesis that its molecular structural/orientational changes, related to the S-BPP bound to the nanoparticle, are driving the changes observed in the Raman

spectrum with temperature. Both the magnitude and the reversibility of the Raman changes observed with temperature effectively preclude the possibility that the actual binding mode to the nanoparticle is changing. The extensive lateral interactions characteristics of alkanethiol-nanoparticles arrays make them more tightly packed than S-BPP. Therefore S-BPP is more prone to random orientation and with more freedom to reorient at the nanoparticle interface promoted by temperature. The observed spatial flexibility of the thiol anchored S-BPP ligands is of interest for molecule chelation purposes, as it should facilitate the envisioned of Fe^{2+} metal ions complexation.

5.7 Conductance measurements on a multilayered Au-NP-S-BPP network

Charge transport in Au-NP-S-BPP network devices provides additional experimental insight into the question of thermal stability of the nanoparticles architecture. Here, not only the S-BPP molecules, but also the nanoparticles are expected to play a role. At low temperatures, the thermal energy $k_B T$ becomes comparable to their charging energy, $E_C = e^2/2C$, i.e. the electrostatic energy needed to add an electron onto the metallic nanoparticle (here C is the total capacitance of a nanoparticle in the array and e is the electron charge). In that case, Coulomb blockade will hamper charge transport. Earlier work on alkanethiol-gold nanoparticle networks demonstrated a wide range of charge transport behaviours within the Coulomb-blockade regime [2, 5, 9, 42]. In Chapter 4 the crossover between the sequential tunneling and cotunneling regimes have been studied for alkanethiol networks, as well as for alkanethiol networks with dithiolated OPE-3 bridges [5]. We estimated typical Coulomb blockade charging energies of around 14-17 meV, in correspondence with temperature- and voltage-dependent transport measurements. Hence, in alkanethiol and OPE-based networks Coulomb blockade dominates below 200-250 K, whereas around room temperature, the current-voltage (I - V) characteristics are linear and practically temperature-independent.

The same method as in Chapter 4 is used to investigate charge transport through Au-NP-S-BPP networks. Nanotrench devices are fabricated with a high width-to-length aspect ratio (~ 200) by electron beam lithography and metal lift-off. Through patterning Ti (3 nm)/Au (47 nm), thick electrodes of 20 μm width, separated by a gap of around 100 nm (~ 10 nanoparticles), are created on Si/SiO₂ substrates. The nanoparticle array is transferred onto these electrodes via a PDMS stamp. Samples containing 2D (single

layer) Au-NP-S-BPP arrays typically exhibited very high ($> 100 \text{ G}\Omega$) resistance values. For that reason, multilayers of Au-NP-S-BPP networks (three times an Au-NP-S-BPP array is stamped on the nanotrench device) are used. The data shown below are obtained after full stabilization of the sample, following an initial resistance decrease as a function of time at room temperature. Most likely, the latter is the result of a slow re-ordering process [43-45].

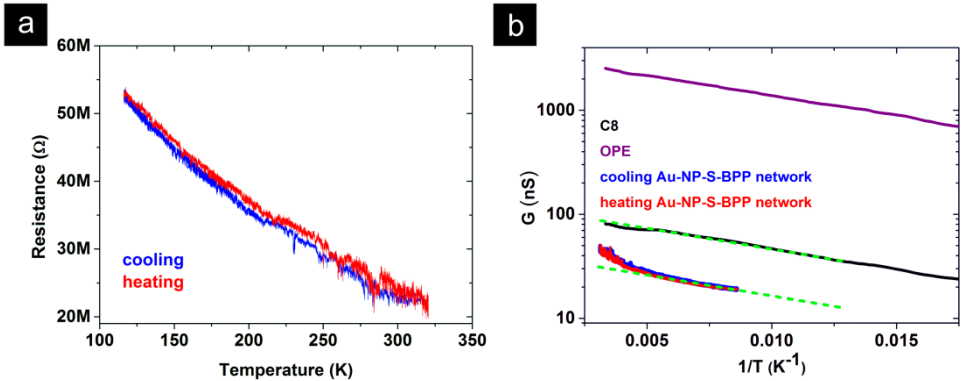


Figure 5.9: (a) Low-bias resistance of a multilayered Au-NP-S-BPP network as a function of temperature for $116 \text{ K} < T < 320 \text{ K}$. Both cooling (black) and heating (red) traces are shown. (b) Arrhenius plot (semilog plot of G versus $1/T$) of the data in Figure 5.9(a) compared to experiments on similar, i.e. three times stamped, C8 networks (black) and OPE-bridged networks (purple). The green dashed lines are parallel guides to the eye to compare the slope for various networks. (For linearly scaled R - T plots see Chapter 6: Figure 6.5(a) for the C8 and Figure 6.5(b) for the OPE case, respectively.)

Figure 5.9(a) shows the low-bias resistance versus temperature for a multilayered Au-NP-S-BPP network microcontact printed on a nanotrench device. The interparticle voltage-bias, typically a factor 10 smaller than the device voltage-bias, is of the order of 3 mV. In Figure 5.9(a), we find that the resistance is monotonically decreasing with temperature for the entire temperature range, without a clear saturation at higher temperatures. If we compare the octanethiol and OPE-based networks with the Au-NP-S-BPP network, however the latter behaves differently at higher temperatures. For example, for the first two types of samples, the low-bias resistance is basically voltage- and temperature-independent at room temperature, indicating that $k_B T_R > E_C$ (see Figures 6.5(a) and 6.5(b)) [5]. However, the I - V curves of the Au-NP-S-BPP network

are surprisingly non-linear (see Appendix B.1). Furthermore, the temperature-dependent behaviour of the low-bias conductance deviates for the Au-NP-S-BPP networks. This becomes most clear in Figure 5.9(b), which shows the data of Figure 5.9(a) in an Arrhenius plot. For comparison the Arrhenius plots for C8 and OPE networks are also displayed. The Arrhenius plots of the C8 and OPE networks point to activated behaviour between 70 K and 300 K, as indicated by the straight-line approximation in Figure 5.9. This is indeed expected for the regime of sequential tunneling (Note that for the lower-temperature cotunneling regime, Efros-Shklovskii behaviour is expected, resulting in an exponential dependence on $T^{0.5}$; see Chapter 4 and [2, 42]). For the three different types of samples, there is actually a clear similarity in the low-temperatures range. This is illustrated by the parallel lines in the semilog plot of Figure 5.9(b), indicating an activation energy of the same order for the three molecular spacers. Nevertheless the Au-NP-S-BPP network sample exhibits a very different behaviour for higher temperatures, showing a clear upturn in the Arrhenius plot (i.e. at lower $1/T$ values in Figure 5.9(b)).

A first explanation for a deviation may be that the charging energy $E_C = e^2/2C \propto C^{-1}$ is actually higher for the Au-NP-S-BPP networks than for alkanethiols networks. This were the case if the nanoparticle radius r and/or the effective dielectric constant ϵ_{eff} around the nanoparticles are considerably lower for the Au-NP-S-BPP networks than for the octanethiol networks (cf. the self-capacitance of a sphere: $C = 4\pi\epsilon_0\epsilon_r r$, see Appendix B.2). However, this is not likely. First, the nanoparticles are made in the same manner for all sets of devices (independent of the molecular species investigated). All the nanoparticles are thus observed to be of similar size. Second, UV-Vis spectroscopy indicates that ϵ_m (and also ϵ_{eff} which incorporates f) is actually higher for Au-NP-S-BPP networks than for alkanethiol networks, consistent with intuition (see Table 1). This should thus lead to a lower charging energy for S-BPP than for octanethiol networks and hence to linear I - V curves at room temperature. Additionally, it is difficult to reconcile a Coulomb-blockade picture with the continuous increase of the slope of the Arrhenius plot of Figure 5.9(b) when heating Au-NP-S-BPP networks. The latter would suggest a significant change of the activation energy, i.e. of the charging energy, as temperature increases. For these reasons, Coulomb blockade is excluded as the reason for the upturn in Figure 5.9(b).

Following the results from temperature-dependent Raman spectroscopy, the proposition can be made that the deviation from simple Arrhenius law behaviour

originates from fluctuations in the molecular interconnects. These fluctuations can result in a modification of the effective tunnel barrier. The gold nanoparticles are here separated by loosely interacting S-BPP molecules, which cannot form a close-packed structure and hence keep room for thermally-driven motions. At higher temperatures, variations in the relative orientation of S-BPP neighbours can result in fluctuations in π - π interactions, yielding changes in charge transfer probability between nanoparticles. In this situation, the effective transmission of the tunnel barrier becomes a time average of the set of all possible configurations each with their own specific transmission value, in a way somewhat similar to the recent proposal in Ref. [46]. For example, temporarily enhanced π - π interaction should lead to higher tunneling probabilities. Time-averaging of such fluctuations may thus result in enhanced transport at high temperatures, explaining the upturn in the Arrhenius plot for the S-BPP network in Figure 5.9(b). One should point out that the transport measurements *per se* do not present a conclusive evidence of disorder-enhanced conductivity of nanoparticles networks. However, the combination of Raman spectroscopy and transport measurements favours such a model, thereby proposing a new approach for understanding how disorder can impact transport properties in molecular junctions. Additional calculations will be required to extend this hypothesis of fluctuations-enhanced transport between the gold nanoparticles, taking into account the percolating character of transport in molecular interconnects arrays. Complementary future experiments may use the conducting-probe AFM or eutectic GaIn methods. In that case, monolayers of S-BPP formed at both electrodes could be gently brought into mechanical contact, after which temperature-dependent $I(V)$ measurements can be done.

5.8 Conclusions

Self-assembled gold nanoparticle arrays, stabilized by a new type of conjugated organic molecules as capping ligands, can be assembled into two-dimensional arrays, which form locally well-ordered structures on different types of substrates. Raman spectroscopy reveals that these S-BPP molecules coordinate selectively to the nanoparticles via thiol-gold bonds, leaving the pyridine and pyrazole available for further chemical binding purposes. Temperature-dependent Raman measurements exhibit frequency shifts for several key modes of the S-BPP molecules, pointing to molecular reorientational changes occurring at high temperatures. The extent of

structural dynamics is far greater than observed for simple alkanethiol modified nanoparticle arrays, and is consistent with the more limited close-packing anticipated for S-BPP. This provides also an explanation for the peculiar temperature dependence of the electrical properties of the S-BPP networks, which shows a clear deviation from Arrhenius behaviour above 220 K. This research suggests that conductance behaviour of molecule-nanoparticle arrays can be tuned as an indicator of dynamical disorder in these structures, which can be a prerequisite to create nanoparticle networks candidate for further chemical functionalization or reactivity. This sets the stage for the attractive possibility of coordinating with Fe^{2+} metal ions, thereby introducing switchable spin transition units into the network.

5.9 References

1. G. M. Whitesides and B. Grzybowski, Self-assembly at All Scales, *Science*, **295**, (2002), 2418-2421.
2. T. B. Tran, I. S. Beloborodov, X. M. Lin, T. P. Bigioni, V. M. Vinokur and H. M. Jaeger, Multiple Cotunneling in Large Quantum Dot Arrays, *Phys. Rev. Lett.*, **95**, (2005), 0768061-0768064.
3. A. Zabet-Khosousi and A.-A. Dhirani, Charge Transport in Nanoparticle Assemblies, *Chem. Rev.*, **108**, (2008), 4072-4124.
4. M. Pauly, J.-F. Dayen, D. Golubev, J.-B. Beaufrand, B. P. Pichon, B. Doudin and S. Bégin-Colin, Co-tunneling Enhancement of the Electrical Response of Nanoparticle Networks, *Small*, **8**, (2012), 108-115.
5. J.-F. Dayen, E. Devid, M. V. Kamalakar, D. Golubev, C. M. Guédon, V. Faramarzi, B. Doudin and S. J. van der Molen, Enhancing the Molecular Signature in Molecule-nanoparticle Networks via Inelastic Cotunneling, *Adv. Mater.*, **25**, (2013), 400-404.
6. R. P. Andres, J. D. Bielefeld, J. I. Henderson, D. B. Janes, V. R. Kolagunta, C. P. Kubiak, W. J. Mahoney and R. G. Osifchin, Self-assembly of a Two-dimensional Superlattice of Molecularly Linked Metal Clusters, *Science*, **273**, (1996), 1690-1693.
7. X. M. Lin, H. M. Jaeger, C. M. Sorensen and K. J. Klabunde, Formation of Long-Range-Ordered Nanocrystal Superlattices on Silicon Nitride Substrates, *J. Phys. Chem. B.*, **105**, (2001), 3353-3357.
8. J. Liao, L. Bernard, M. Langer, C. Schönenberger and M. Calame, Reversible Formation of Molecular Junctions in 2D Nanoparticle Arrays, *Adv. Mater.*, **18**, (2006), 2444-2447.
9. L. Bernard, Y. Kamdzhilov, M. Calame, S. J. van der Molen, J. Liao and C. Schönenberger, Spectroscopy of Molecular Junction Networks Obtained by Place Exchange in 2D Nanoparticle Arrays, *J. Phys. Chem. C*, **111**, (2007), 18445-18450.

10. M. J. Hostetler, A. C. Templeton and R. W. Murray, Dynamics of Place-exchange Reactions on Monolayer-protected Gold Cluster Molecules, *Langmuir*, **15**, (1999), 3782-3789.
11. J. Liao, J. S. Agustsson, S. Wu, C. Schönenberger, M. Calame, Y. Leroux, M. Mayor, O. Jeannin, Y.-F. Ran, S.-X. Liu and S. Decurtins, Cyclic Conductance Switching in Networks of Redox-active Molecular Junctions, *Nano Lett.*, **10**, (2010), 759-764.
12. S. J. van der Molen, J. Liao, T. Kudernac, J. S. Agustsson, L. Bernard, M. Calame, B. J. van Wees, B. L. Feringa and C. Schönenberger, Light-controlled Conductance Switching of Ordered Metal-Molecule-Metal Devices, *Nano Lett.*, **9**, (2009), 76-80.
13. A. Kaminska, O. Inya-Agha, R. J. Forster and T. E. Keyes, Chemically Bound Gold Nanoparticle Arrays on Silicon: Assembly, Properties and SERS Study of Protein Interactions, *Phys. Chem. Chem. Phys.*, **10**, (2008), 4172-4180.
14. M. Halcrow, The Synthesis and Coordination Chemistry of 2,6-bis(pyrazolyl)pyridines and Related Ligands - Versatile Terpyridine Analogues, *Coord. Chem. Rev.*, **249**, (2005), 2880-2908.
15. C. Rajadurai, F. Schramm, S. Brink, O. Fuhr, M. Ghafari, R. Kruk and M. Ruben, Spin Transition in a Chainlike Supramolecular Iron(II) Complex, *Inorg. Chem.*, **45**, (2006), 1019-1021.
16. M. Cavallini, I. Bergenti, S. Militta, J. C. Kengne, D. Gentili, G. Ruani, I. Šalitroš, V. Meded and M. Ruben, Thin Deposits and Patterning of Room-Temperature-Switchable One-dimensional Spin-crossover Compounds, *Langmuir*, **27**, (2011), 4076-4081.
17. V. Meded, A. Bagrets, K. Fink, R. Chandrasekar, M. Ruben, F. Evers, A. Bernard-Mantel, J. S. Seldenthuis, A. Beukman and H. S. J. van der Zant, Electrical Control over the Fe(II) Spin Crossover in a Single Molecule: Theory and Experiment, *Phys. Rev. B*, **83**, (2011), 245415(1-13).
18. R. Chandrasekar, F. Schramm, O. Fuhr and M. Ruben, An Iron(II) Spin-transition Compound with Thiol Anchoring Groups, *Eur. J. Inorg. Chem.*, **17**, (2008), 2649-2653.
19. M. Kamenetska, S. Y. Quek, A. C. Whalley, M. L. Steigerwald, H. J. Choi, S. G. Louie, C. Nuckolls, M. S. Hybertsen, J. B. Neaton and L. Venkataraman, Conductance and Geometry of Pyridine-linked Single-molecule Junctions, *J. Am. Chem. Soc.*, **132**, (2010), 6817-6821.
20. C. M. Guédon, J. Zonneveld, H. Valkenier, J. C. Hummelen and S. J. van der Molen, Controlling the Interparticle Distance in a 2D Molecule-nanoparticle Network, *Nanotechnology*, **22**, (2011), 125205(1-5).
21. R. G. Nuzzo and D. L. Allara, Adsorption of Bifunctional Organic Disulfides on Gold Surfaces, *J. Am. Chem. Soc.*, **105**, (1983), 4481-4483.
22. J. M. Tour, L. Jones II, D. L. Pearson, J. J. S. Lamba, T. P. Burgin, G. M. Whitesides, D. L. Allara, A. N. Parikh and S. Atre, Self-assembled Monolayers and Multilayers of Conjugated Thiols, .alpha.,.omega.-Dithiols, and Thioacetyl-containing Adsorbates. Understanding Attachments between Potential Molecular Wires and Gold Surfaces, *J. Am. Chem. Soc.*, **117**, (1995), 9529-9534.

-
23. S. Huang, G. Tsutsui, H. Sakaue, S. Shingubara and T. Takahagi, Experimental Conditions for a Highly Ordered Monolayer of Gold Nanoparticles Fabricated by the Langmuir-Blodgett Method, *J. Vac. Sci. Technol. B*, **19**, (2001), 2045-2049.
 24. V. Santhanam and R. P. Andres, Microcontact Printing of Uniform Nanoparticle Arrays, *Nano Lett.*, **4**, (2004), 41-44.
 25. J.-F. Dayen, V. Faramarzi, M. Pauly, N. T. Kemp, M. Barbero, B. P. Pichon, H. Majjad, S. Begin-Colin and B. Doudin, Nanotrench for Nano and Microparticle Electrical Interconnects, *Nanotechnology*, **21**, (2010), 335303(1-7).
 26. P. A. Midgley, M. Weyland, J. M. Thomas and B. F. G. Johnson, Z-contrast Tomography: a Technique in Three-dimensional Nanostructural Analysis based on Rutherfordscattering, *Chem. Commun.*, **10**, (2001), 907-908.
 27. C. Kübel, A. Voigt, R. Schoenmakers, M. Otten, D. Su, T.-C. Lee, A. Carlsson and J. Bradley, Recent Advances in Electron Tomography: TEM and HAADF-STEM Tomography for Materials Science and Semiconductor Applications, *Microsc. & Microanal.*, **11**, (2005), 378-400.
 28. J. Kumar, X. Wei, S. Barrow, A. M. Funston, K. G. Thomas and P. Mulvaney, Surface Plasmon Coupling in End-To-End Linked Gold Nanorod Dimers and Trimers, *Phys. Chem. Chem. Phys.*, **15**, (2013), 4258-4264.
 29. G. Mie, Beiträge Zur Optik Trüber Medien, Speziell Kolloidaler Metallösungen, *Ann. Phys.*, **25**, (1908), 377-445.
 30. L. Bernard, *Expanding the Horizon of Molecular Electronics via Nanoparticle Assemblies*. Ph. D. Thesis, University of Basel, Switzerland, **2006**.
 31. J. M. Garnett, Colours in Metal Glasses and in Metallic Films, *Philos. Trans. R. Soc. London*, **203**, (1904), 385-420.
 32. R. W. Cohen, G. D. Cody, M. D. Coutts and B. Abeles, Optical Properties of Granular Silver and Gold Films, *Phys. Rev. B*, **8**, (1973), 3689-3701.
 33. D. Dalascu and L. Martinu, Optical Properties of Discontinuous Gold Films: Finite-size Effects, *Journal of the Optical Society of America B: Optical Physics*, **18**, (2001), 85-92.
 34. N. Camillone III, T. Y. B. Leung, P. Schwartz, P. Eisenberger and G. Scoles, Chain Length Dependence of the Striped Phases of Alkanethiol Monolayers Self-assembled on Au(111): An Atomic Beam Diffraction Study, *Langmuir*, **12**, (1996), 2737-2746.
 35. S. K. Saikin, R. Olivares-Amaya, D. Rappoport, M. Stopa and A. Aspuru-Guzik, On the Chemical Bonding Effects in the Raman Response: Benzenethiol Adsorbed on Silver Clusters, *Phys. Chem. Chem. Phys.*, **11**, (2009), 9401-9411.
 36. K. B. Biggs, J. P. Camden, J. N. Anker and R. P. van Duyne, Surface-enhanced Raman Spectroscopy of Benzenethiol Adsorbed from the Gas Phase onto Silver Film over Nanosphere Surfaces: Determination of the Sticking Probability and Detection Limit Time, *J. Phys. Chem. A.*, **113**, (2009), 4581-4586.
 37. X. W. Kang and S. W. Chen, Electronic Conductivity of Alkyne-capped Ruthenium Nanoparticles, *Nanoscale*, **4**, (2012), 4183-4189.
 38. G. Cardini and M. Muniz-Miranda, Density Functional Study on the Adsorption of Pyrazole onto Silver Colloidal Particles, *J. Phys. Chem. B.*, **106**, (2002), 6875-6880.
 39. F. Lordan, N. Al-Attar, C. Mallon, J. Bras, G. Collet, R. J. Forster, T. E. Keyes and J. H. Rice, Temperature Dependence of a_1 and b_2 Type Modes in the Surface

- enhanced Raman from 4-Aminobenzenethiol, *Chemical Physics Letters*, **556**, (2013), 158-162.
40. H. Yan, S. I. Lim, L.-C. Zhang, S.-C. Gao, D. Mott, Y. Le, R. Loukrakpam, D.-L. An and C.-J. Zhong, Rigid, Conjugated and Shaped Arylethynes as Mediators for the Assembly of Gold Nanoparticles, *J. Mater. Chem.*, **21**, (2011), 1890-1901.
41. S. Eisler, R. McDonald, G. R. Loppnow and R. R. Tykwinski, Structural, Vibrational, and Electronic Characteristics of Enyne Macrocycles as a Function of Ring Strain, *J. Am. Chem. Soc.*, **122**, (2000), 6917-6928.
42. T. B. Tran, I. S. Beloborodov, J. Hu, X. M. Lin, T. F. Rosenbaum and H. M. Jaeger, Sequential Tunneling and Inelastic Cotunneling in Nanoparticle Arrays, *Phys. Rev. B.*, **78**, (2008), 075437-075445.
43. A. N. Shipway, E. Katz and I. Willner, Nanoparticle Arrays on Surfaces for Electronic, Optical, and Sensor Applications, *Chemphyschem*, **1**, (2000), 18-52.
44. G. Schmid, St. Peschel and Th. Sawitowski, Two-dimensional Arrangements of Gold Clusters and Gold Colloids on Various Surfaces, *Z. anorg. allg. Chem.*, **623**, (1997), 719-723.
45. T. Sato, D. Brown and B. F. G. Johnson, Nucleation and Growth of Nano-gold Colloidal Lattices, *Chem. Commun.*, **0**, (1997), 1007-1008.
46. C. George, I. Szleifer and M. Ratner, Multiple-Time-Scale Motion in Molecularly Linked Nanoparticle Arrays, *ACS Nano*, **7**, (2013), 108-116.
47. J. Slot and H. Geuze, A New Method for Preparing Gold Probes for Multiple Labeling Cytochemistry, *Eur. J. Cell Biol.*, **38**, (1985), 87-93.
48. Y. Noguchi, T. Terui, T. Katayama, M. M. Matsushita and T. Sugawara, Charge Transport in Various Dimensions of Small Networks Composed of Gold Nanoparticles and Terthiophene Wire-molecules, *Appl. Phys. Lett.*, **98**, (2011), 263114-263117.
49. M. Allen, Coulomb Blockade in Network of Nanoparticles, *Matter, Geometry, and Electromagnetics*, S-96, **4620**, (2006), 1-9.
